

Frustration-induced magnetic bimerons in transition metal halide CoX_2 ($\text{X} = \text{Cl}, \text{Br}$) monolayers

Yu Wang, Shuai Dong and Xiaoyan Yao*

Key Laboratory of Quantum Materials and Devices of Ministry of Education,
School of Physics, Southeast University, Nanjing 211189, China

Abstract

With the field of two-dimensional (2D) magnetic materials expanding rapidly, noncollinear topological magnetic textures in 2D materials are attracting growing interest recently. As the in-plane counterpart of magnetic skyrmions, magnetic bimerons have the same topological advantages, but are rarely observed in experiments. Employing first-principles calculations and Monte Carlo simulations, we predict that the centrosymmetric transition metal halide CoX_2 ($\text{X} = \text{Cl}, \text{Br}$) monolayers can be promising candidates for observing the frustration-induced bimerons. These bimerons crystallize into stable triangular lattice under an appropriate magnetic field. Compared to the skyrmions driven by the Dzyaloshinskii-Moriya interaction or the long-ranged magnetic dipole-dipole interactions, these frustration-induced bimerons have much smaller size and flexible tunability. Furthermore, the biaxial strain provides an effective method to tune the frustration and thereby to tune the bimeron lattice. In detail, for CoCl_2 monolayer, tensile strain can be applied to generate bimeron lattice, further shrink bimeron size and increase the density of bimerons. For CoBr_2 monolayer with inherent bimeron lattice state, a unique orientation rotation of bimeron lattice controlled by compressive strain is predicted.

Keywords: bimeron, topological magnetic texture, frustration, transition metal halide, strain modulation

1 Introduction

Two-dimensional (2D) van der Waals (vdW) materials in the atomic thickness limit with high tunability and peculiar quantum properties have been significantly highlighted in recent years [1, 2]. Among them, the 2D materials with intrinsic magnetism are particularly intriguing due to plentiful technological opportunities, such as information storage, spintronics and sensing devices [3-5]. Since the first observations of intrinsic ferromagnetism in $\text{Cr}_2\text{Ge}_2\text{Te}_6$ [6] and CrI_3 [7] in 2017, the field of 2D magnetic materials expanded rapidly. The intrinsic magnetism has been confirmed experimentally in a variety of 2D materials, for example, ferromagnetism in Fe_3GeTe_2 [8] and MnSe_2 [9], while antiferromagnetism in FePS_3 [10] and CrTe_2 [11]. By calculations, more 2D materials have been predicted as promising candidates with intrinsic magnetism, such as GdI_2 [12], CrOX ($\text{X} = \text{Cl}, \text{Br}$) [13], Mn_3X_4 ($\text{X} = \text{Te}, \text{Se}$) [14] and so on. Meanwhile, diversified novel phenomena, e.g. multiferroicity, ferrovalley and quantum anomalous Hall effect, have been observed or predicted in these 2D magnetic materials [4, 15-18].

In the field of magnetism, noncollinear magnetic textures with topological untrivial property attracted growing interest for both theoretical and experimental activities [19-21]. In particular, magnetic skyrmions were much highlighted due to its potential applications for nonvolatile energy-efficient spintronic devices [20, 22-24]. It is noteworthy that the skyrmion may show different morphologies under the topological protection, which could be generally called skyrmionic magnetic textures. As an in-plane topological counterpart of skyrmion, the magnetic bimeron has the same advantages, such as topological stability, small size and low driving current density [19, 23, 25]. (Note that bimeron may also refer to "elongated skyrmions" [26-29], which are different from the bimeron in the present paper.) Meanwhile, bimerons are highly desirable due to their unique properties different from skyrmions, for instance, they allow for a pure topological Hall effect upon variation of the in-plane field [19, 30], and they may move without skyrmion Hall effect with a specific current direction [31]. It was first predicted in 2017 that bimeron could exist in an asymmetric form in chiral magnets [32, 33], and also in a symmetric form in the frustrated system [34]. However, compared with the plentiful investigations of

skyrmions, bimerons are rarely observed in experiments. Up to now, only isolated bimerons have been observed experimentally [19], for example, the bimeron-like bubbles were observed in single-crystalline Fe/Ni bilayers grown on a W(110) crystal [35], a bimeron was generated in a Py film by local vortex imprinting from a Co disk [36], and recently the antiferromagnetic bimeron was stabilized in α -Fe₂O₃ capped with a platinum overlayer [37].

As natural excitations of ferromagnet in 2D space, skyrmionic magnetic textures are much expected to exist in 2D magnetic materials, and the previous experiments demonstrated that the reduction of materials' dimension is beneficial to the stability of skyrmions [38, 39]. It was inspiring that skyrmions had been observed experimentally in the 2D vdW Cr₂Ge₂Te₆ and Fe₃GeTe₂ [40, 41]. Very recently, room-temperature skyrmion lattice was also reported in experiment of 50% Co-doped Fe₅GeTe₂ [42]. On the other hand, different methods were discussed theoretically to generate and modulate skyrmions in 2D magnetic materials [43]. In particular, Janus Cr(I, Cl)₃, and polar VOI₂ monolayers were predicted to possess Dzyaloshinskii-Moriya interaction (DMI), and thus the bimeron state could be stabilized [44, 45]. Recently, bimerons were also predicted in some vdW heterostructures with DMI [46, 47] and multiferroic LaBr₂ bilayer [48].

The frustration of exchange interactions is another important mechanism for skyrmions [49, 50]. In centrosymmetric materials, the frustration-induced skyrmionic magnetic textures may possess more internal degrees of freedom [51, 52]. The stable magnetic textures with different topological charges may coexist, allowing for more advanced logical operations. Compared to the size of several hundred nanometers for most skyrmions driven by DMI or dipole-dipole interaction, the frustration-induced skyrmionic textures are usually much smaller, about several nanometers in size, and thus the higher density may contribute to stronger topological Hall effect [53, 54]. It is pity that the frustration-induced skyrmionic magnetic textures have rarely been reported in 2D materials up to now. The frustration-induced skyrmions and anti-biskyrmions were predicted in vdW NiI₂ monolayer [55]. The static and dynamic properties of an isolated bimeron in frustrated ferromagnetic monolayer were studied numerically [56], but the realization of bimerons in real 2D materials remains unsolved and worth more investigation.

In this work, via first-principles calculations and Monte Carlo simulations, we unveil that the frustration-induced bimeron lattice could be realized in 2D centrosymmetric CoX₂ (X = Cl, Br) monolayers under appropriate magnetic field. Furthermore, biaxial strain provides an efficient approach to tune the frustration and thus to tune these bimerons. For CoCl₂ monolayer, although ferromagnetism dominates, tensile strain can be applied to strengthen frustration and thus induce bimeron lattice. For CoBr₂ monolayer with inherent bimeron state, compressive strain may modulate frustration and thus to control the density of bimerons. In particular, it is intriguing that compressive strain can even control the orientation of bimeron lattice in an angle range of 30°.

2 Calculation methods

First-principles calculations are performed within the density functional theory (DFT) framework, as implemented in the Vienna *ab initio* Simulation Package (VASP) [57]. The core electrons are treated by the projector augmented wave (PAW) method [58], and the Perdew-Burke-Ernzerhof (PBE) version of the generalized gradient approximation (GGA) is used for structure optimization, electronic structure, and magnetism calculation [59]. The plane-wave cutoff energy is set to be 550 eV. The structures are fully relaxed with the conjugate gradient method until the maximum force is less than 1 meV/Å on each atom, and the total energy converges to 10⁻⁶ eV. For bulk calculation, the vdW correction is described by Many-body dispersion energy method [60, 61]. For monolayer calculations, a vacuum region of approximately 20 Å is added in the perpendicular direction to eliminate spurious interaction between periodic replicas. To sample the Brillouin zone, a k-mesh density of 60/a₀ is applied along in-plane directions, where a₀ denotes in-plane lattice constant. The phonon spectrum is calculated based on the density functional perturbation theory (DFPT) [62, 63]. The *ab initio* molecular dynamics (AIMD) simulation in the canonical ensemble lasts for 3000 fs with a time step of 1 fs at 300 K. The magnetic anisotropy energy (MAE) is calculated with the spin-orbit coupling (SOC) considered.

Furthermore, the Markov-chain Monte Carlo (MC) simulations of the Metropolis algorithm combined with the over-relaxation method are performed on triangular lattice with periodic boundary conditions to study the noncollinear spin textures [64, 65]. The system is first evolved from a relatively high temperature to a very low temperature gradually, and then the energy is further minimized by only accepting the update with the energy reduction to approach zero temperature. The stable magnetic state with the lowest energy is obtained by comparing independent datasets evolving from different initial states on the lattices of different sizes (from 1296 to 5184 sites). And then the bimeron state can be identified from these stable magnetic states by the following analyses.

To characterize the spin (\mathbf{S}) configuration, the spin structure factor is evaluated for three spin components ($\gamma = x, y$ and z) respectively as follows:

$$\mathbf{S}^\gamma(\mathbf{q}) = \sum_{i,j} e^{iq \cdot (\mathbf{r}_j - \mathbf{r}_i)} \langle \mathbf{S}_i^\gamma \cdot \mathbf{S}_j^\gamma \rangle \quad (1)$$

The topological property of magnetic texture is confirmed by topological charge Q , namely,

$$Q = \frac{1}{4\pi} \iint \mathbf{S} \cdot (\partial_x \mathbf{S} \times \partial_y \mathbf{S}) dx dy \quad (2)$$

which quantifies the times \mathbf{S} wrapping around a unit sphere as the coordinate (x, y) spans the defined region. If $Q=1$ for each isolated skyrmionic magnetic texture, then the topological charge of whole lattice is just the number of skyrmionic magnetic textures. In this work, the isolated bimerons induced by frustration with topological charge $Q = \pm 1$ are degenerate in energy. To further locate and characterize the topological magnetic textures, the local topological charge density $\rho(\mathbf{r})$ is evaluated as follows:

$$\rho(\mathbf{r}) = \frac{1}{4\pi} \mathbf{S} \cdot (\partial_x \mathbf{S} \times \partial_y \mathbf{S}) \quad (3)$$

In simulation, Q and $\rho(\mathbf{r})$ are calculated for a discrete spin lattice in the manner of Ref [66].

3 Results

In recent years, transition metal dihalides and trihalides with 2D vdW layered structure attracted considerable attention [67]. Among them, bulk CoCl_2 and CoBr_2 were synthesized and studied experimentally [68-71]. The stable existence of their monolayers were predicted by later calculations [72-74]. The calculation on basic magnetic properties indicated that for both CoCl_2 and CoBr_2 the energy of ferromagnetic (FM) order is lower than that of antiferromagnetic (AFM) state, and the magnetism can be controlled via various methods [73, 74]. Since the energy difference between FM and AFM states is relatively small, the more complicated noncollinear magnetic order can be expected.

For the calculation of CoX_2 bulks, the Hubbard U -correction on the $3d$ orbitals of Co is considered, comparing to the calculation without U . It is demonstrated that the in-plane Co-Co distance and the layer spacing without U are more consistent with the experimental data [67-69]. Please see Note 1 in the Supplementary material for details. Note that the previous DFT calculations without U also successfully reproduced the lattice parameters and electronic structures of transition metal halides [72, 75-77]. Therefore, the subsequent results are obtained by the DFT calculation without U . It must be clarified that we also perform the calculations of CoX_2 monolayers with effective $U = 3$ eV applied, and the results remain qualitatively the same. Please see Note 5 in the Supplementary material for details. Due to the weak interlayer vdW interaction, the cleavage energy (E_{cl}) calculated by using four-layer slab method [78] is only about 0.15 J/m^2 for both CoCl_2 and CoBr_2 (Please see Note 2 in the Supplementary material), which is much smaller than that of graphite ($0.39 \pm 0.02 \text{ J/m}^2$) [79]. Thus, it is feasible to exfoliate the CoCl_2 and CoBr_2 monolayers from their bulks.

CoX_2 ($X = \text{Cl, Br}$) monolayer possesses a centrosymmetric crystal structure as shown in Fig. 1(a) and 1(b). From the side view, the monolayer contains Co atomic layer sandwiched by two halogen atomic layers. From the top view, Co^{2+} cations in edge sharing X octahedra construct a triangular net. The relaxed lattice constants a_0 of monolayers are summarized in Table 1, consistent well with the previous reports [73, 74].

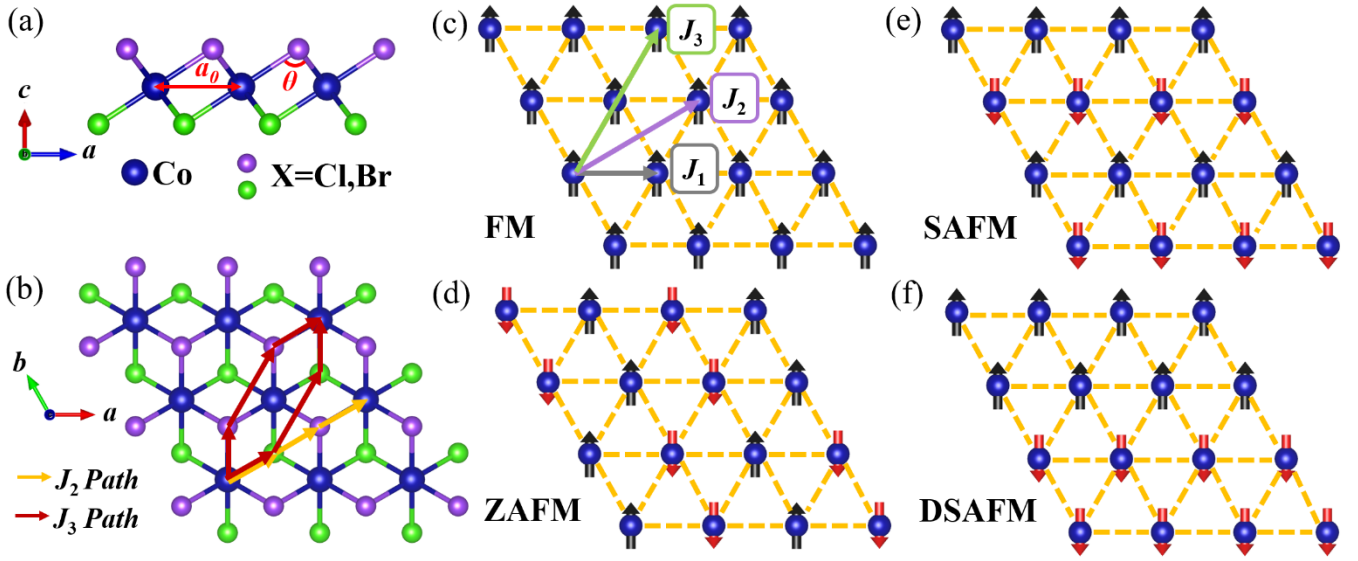


Fig. 1 The crystal structure of CoX_2 ($X = \text{Cl}, \text{Br}$) monolayer. (a) The side view where the lattice constant and Co-X-Co bond angle are denoted by a_0 and θ , respectively. (b) The top view where Co atoms form an equilateral triangular structure. The X ions in the top and bottom layers are differentiated by green and purple colors. The arrows sketch the possible paths for the second-neighboring and the third-neighboring exchange interactions. (c)-(f) Four basic magnetic orders, namely, (c) Ferromagnetic (FM), (d) Zigzag antiferromagnetic (ZAFM), (e) Stripe antiferromagnetic (SAFM), and (f) Double-stripe antiferromagnetic (DSAFM) configurations.

Table 1 Calculated lattice constant a_0 , Co-X-Co bond angle θ , magnetic moment m of Co and X atoms, band gap E_g without and with SOC.

Units	a_0 (Å)	θ (deg)	m (Co) (μ_B)	m (X) (μ_B)	E_g (eV)	E_g (SOC) (eV)
CoCl_2	3.545	93.240	2.517	0.173	0.369	0.366
CoBr_2	3.748	92.680	2.460	0.188	0.373	0.400

The calculation on the mechanical properties of monolayer CoX_2 indicates that the elastic constants meet elastic stability criteria, suggesting their mechanical stability [80, 81]. The calculated Young's moduli are 29.687 N/m for CoCl_2 and 28.712 N/m for CoBr_2 , which are much smaller than that of graphene (340 N/m) with good mechanical flexibility [82, 83]. The gravity-induced out-of-plane deformation estimated by elasticity theory shows that the monolayer CoX_2 could withstand its own weight and preserve the planar structure during the process of exfoliation [78, 84]. The dynamical stability is verified by phonon spectra without imaginary frequencies, and the thermal stability is confirmed by AIMD simulation. Please see Note 3 in the Supplementary material for details.

Under the influence of octahedral crystal field, the $3d$ orbitals of transition metal atom always split into higher energy level e_g ($d_{x^2-y^2}, d_z^2$) and lower energy level t_{2g} (d_{xy}, d_{xz}, d_{yz}). Thus Co^{2+} ion (d^7) has two possible states: high-spin ($S = 3/2$) and low-spin ($S = 1/2$). For both CoCl_2 and CoBr_2 , the high-spin state is preferred as shown in Table 1, which has been confirmed by neutron diffraction and previous calculations [71, 85]. As presented in the band structures of Fig. 2, CoCl_2 and CoBr_2 are both semiconductors, consistent with previous reports [74]. The indirect band gaps are ~ 0.37 eV for both CoCl_2 and CoBr_2 . It is obvious that Co- d orbitals hybridize with X- p orbitals near the Fermi level. The SOC has weak effect on electronic structures and the band gap only changes a little (Table 1 and Note 4 of the Supplementary material).

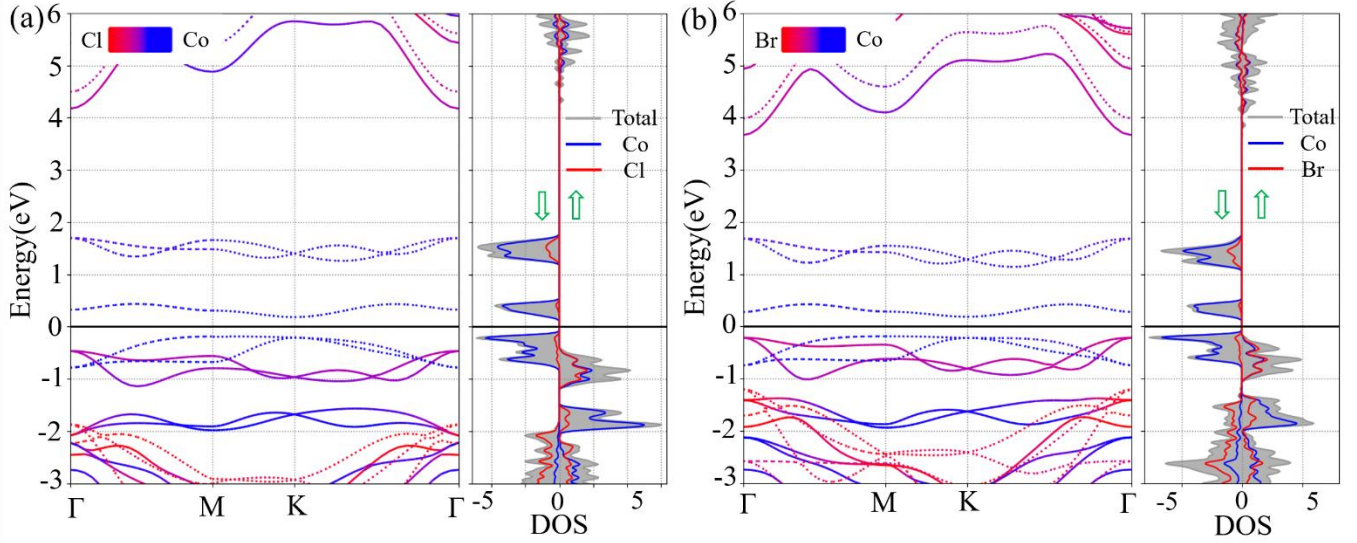


Fig. 2 Atom-resolved band structures and density of states (DOS) for (a) CoCl₂ and (b) CoBr₂ monolayers. The solid line represents spin up and the dotted line represents spin down in band structures. The green arrows in DOS indicate spin up and down respectively. The Fermi level is set to 0 eV.

To describe the magnetism of CoX₂ monolayer, the classic Heisenberg spin model can be constructed and the Hamiltonian can be written as:

$$H = J_1 \sum_{\langle i,j \rangle} \mathbf{S}_i \cdot \mathbf{S}_j + J_2 \sum_{\langle\langle i,m \rangle\rangle} \mathbf{S}_i \cdot \mathbf{S}_m + J_3 \sum_{\langle\langle\langle i,n \rangle\rangle\rangle} \mathbf{S}_i \cdot \mathbf{S}_n + k \sum_i (\mathbf{S}_i^z)^2 + \mathbf{h} \cdot \sum_i \mathbf{S}_i \quad (4)$$

where \mathbf{S}_i represents the normalized classic spin ($|\mathbf{S}| = 1$). On the right of Eq. (4), the first three terms describe the exchange energies. J_1 , J_2 , and J_3 are the nearest-neighboring, second-neighboring, and third-neighboring exchange couplings. The fourth and fifth terms describe the energies of uniaxial anisotropy (k : magnetic anisotropic coefficient) and magnetic field (\mathbf{h}), respectively. Recently, the similar J_1 - J_2 - J_3 models in the triangular lattice were studied to show AFM skyrmions [86, 87]. In addition, meron/antimeron-like lattice textures were observed in the frustrated honeycomb model with triangular sublattices [88].

To extract the exchange couplings, four basic magnetic orders are considered, namely Ferromagnetic (FM), Zigzag antiferromagnetic (ZAFM), Stripe antiferromagnetic (SAFM) and Double-stripe antiferromagnetic (DSAFM) configurations, as sketched in Fig. 1(c-f). By mapping the DFT energies of these magnetic orders to aforementioned Hamiltonian, J_1 , J_2 , and J_3 can be obtained as following

$$\begin{aligned} E_{FM} &= E_0 + 3J_1 + 3J_2 + 3J_3 \\ E_{ZAFM} &= E_0 - J_1 + J_2 - J_3 \\ E_{SAFM} &= E_0 - J_1 - J_2 + 3J_3 \\ E_{DSAFM} &= E_0 + J_1 - J_2 - J_3 \end{aligned} \quad (5)$$

where E_0 denotes the energy of nonmagnetic part. The calculated values of J_1 , J_2 , and J_3 are summarized in Table 2. It is indicated that both CoCl₂ and CoBr₂ show FM J_1 ($J_1 < 0$) together with AFM J_2 and J_3 ($J_2 > 0$, $J_3 > 0$). According to the Goodenough-Kanamori-Anderson (GKA) rules [89-91], the FM J_1 mainly derives from the super-exchange interaction between the $3d$ orbitals of neighbouring Co atoms via overlapping X- p orbitals, where the Co-X-Co bond angle θ is close to 90° for both CoCl₂ and CoBr₂ (Table 1). J_2 and J_3 are both AFM, since they could be considered as super-super-exchange coupling via the p orbitals of two X anions [92]. As discussed in Ref. [92] and sketched in Fig.

1(b), J_3 involves two X anions on the same plane, and thus a stronger X-X hybridization, and hence $J_3 > J_2$. CoCl₂ has dominant J_1 and thus relatively strong ferromagnetism, while CoBr₂ possesses J_3 comparable to J_1 , and thus a strong magnetic frustration between exchange interactions. For MAE, the magnetic anisotropic coefficient k is calculated by $E_{\text{oop}} - E_{\text{ip}}$, where E_{oop} and E_{ip} are the FM energies per Co atom with the magnetization along the out-of-plane and in-plane directions respectively. The calculation indicates that CoCl₂ has an easy-axis anisotropy ($k < 0$), whereas CoBr₂ owns an easy-plane one ($k > 0$) as shown in Table 2. The k of CoBr₂ is much larger than that of CoCl₂, since the MAE of transition metal halides usually arises predominantly from the SOC in halogen atoms [93].

Table 2 The exchange coefficients J_1, J_2, J_3 and magnetic anisotropic coefficient k

	J_1 (meV)	J_2 (meV)	J_3 (meV)	k (meV)
CoCl ₂	-4.188	0.073	1.229	-0.015
CoBr ₂	-1.906	0.110	1.910	0.575

Considering the flexibility of CoCl₂ and CoBr₂ monolayers, strain provides a powerful approach to tune the magnetic properties. Here, an in-plane biaxial strain is applied, which is described as $\varepsilon = (a - a_0)/a_0$, where a_0 and a represent the in-plane lattice constants of pristine and strained monolayers. Aiming at the relatively strong ferromagnetism in CoCl₂ and frustration in CoBr₂, tensile and compressive strains are applied respectively. In the strain range applied here, $J_1 < 0$ and $J_2, J_3 > 0$ are always kept for both CoCl₂ and CoBr₂ monolayers.

For CoCl₂ monolayer, when the tensile strain ($\varepsilon > 0$) is raised, J_2 and J_3 decrease slightly, while J_1 rises obviously as shown in Fig. 3(a). All the three exchange interactions are weakened as the Co-Co distance is stretched. Meanwhile, the Co-Cl-Co bond angle θ increases from 93.24° to 96.94°, corresponding to the weakening J_1 , consistent with the GKA rules [89-91], i.e. the superexchange interaction prefers FM when the cation-anion-cation bond angle is closer to 90°. Although both J_2 and J_3 are reduced in magnitude by applying tensile strain, the ratio $|(J_2 + J_3)/J_1|$ increases as plotted in Fig. 3(b), which ensures the enhancement of frustration. In addition, the magnetic anisotropic coefficient k also changes as the strain is applied, namely the easy direction transfers from out-of-plane to in-plane, as illustrated in Fig. 3(c).

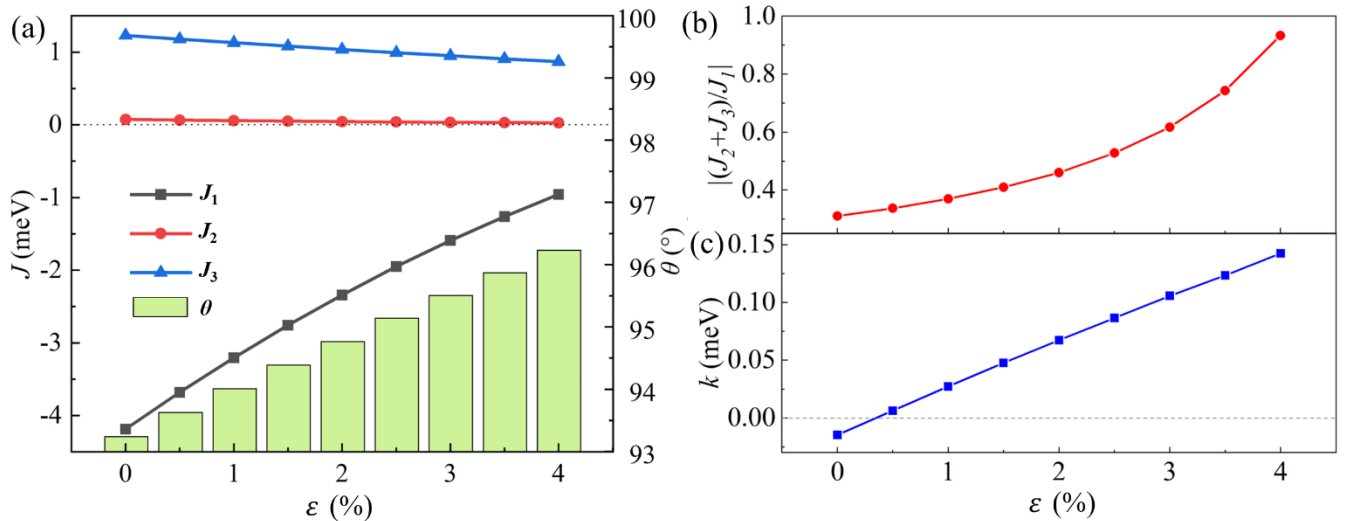


Fig. 3 The effect of tensile strain on CoCl₂ monolayer. (a) The exchange coefficients J_1, J_2, J_3 and Co-Cl-Co bond angle θ , (b) the ratio $|(J_2 + J_3)/J_1|$, and (c) the magnetic anisotropic coefficient k as a function of the tensile strain.

In general, the easy-plane anisotropy tends to produce magnetic bimerons [34]. Based on the first-principles parametrized Heisenberg model, the MC simulations are performed. An in-plane magnetic field \mathbf{h} is applied along x-axis,

because a perpendicular magnetic field is usually required to stabilize skyrmions and a bimeron can be obtained from a skyrmion by 90° rotation around an in-plane axis [30]. The results show that bimerons can be stabilized in CoCl_2 monolayer when the tensile strain is applied. As demonstrated in Fig. 4(a), with the strain further increasing, the h -window of stable bimeron state with the lowest energy expands, owing to the enhancement of frustration between exchange interactions. Meanwhile, the spiral state exists under the magnetic field lower than that of bimeron region [94].

The real-space spin textures obtained in MC simulation are displayed in Fig. 4(d). Each bimeron is characterized as a meron–antimeron pair with opposite polarities, just corresponding to a region with non-zero local topology charge density $\rho(r)$, as marked in Fig. 4(d). The bimerons form a triangular lattice, corresponding to the typical triple- q spin structure factor with sharp peaks on the corners of a hexagon for S^y+S^z , and together with the center for S^x , as presented in Fig. 4(b), in contrast to the double- q spin structure factor of meron-antimeron lattices [19, 95]. The strain can effectively modulate the density of bimerons and the size of each bimeron by tuning the frustration. When the tensile strain is raised, the density of bimerons increases gradually [Fig. 4(d)]. Correspondingly, the spin structure factor presents d_p (the distance between the peaks at corner and center) increasing with strain ε . Meanwhile the area of a single bimeron declines, and it reaches as small as about 2.307 nm^2 when tensile strain reaches 4%, as shown in Fig. 4(c), which is much smaller than most skyrmions driven by DMI or dipole-dipole interaction. Therefore, the frustration is advantageous in producing more compact noncollinear topological textures, and it can be controlled by strain to tune their density and size, which is in line with the pursuit of higher density and better applicability.

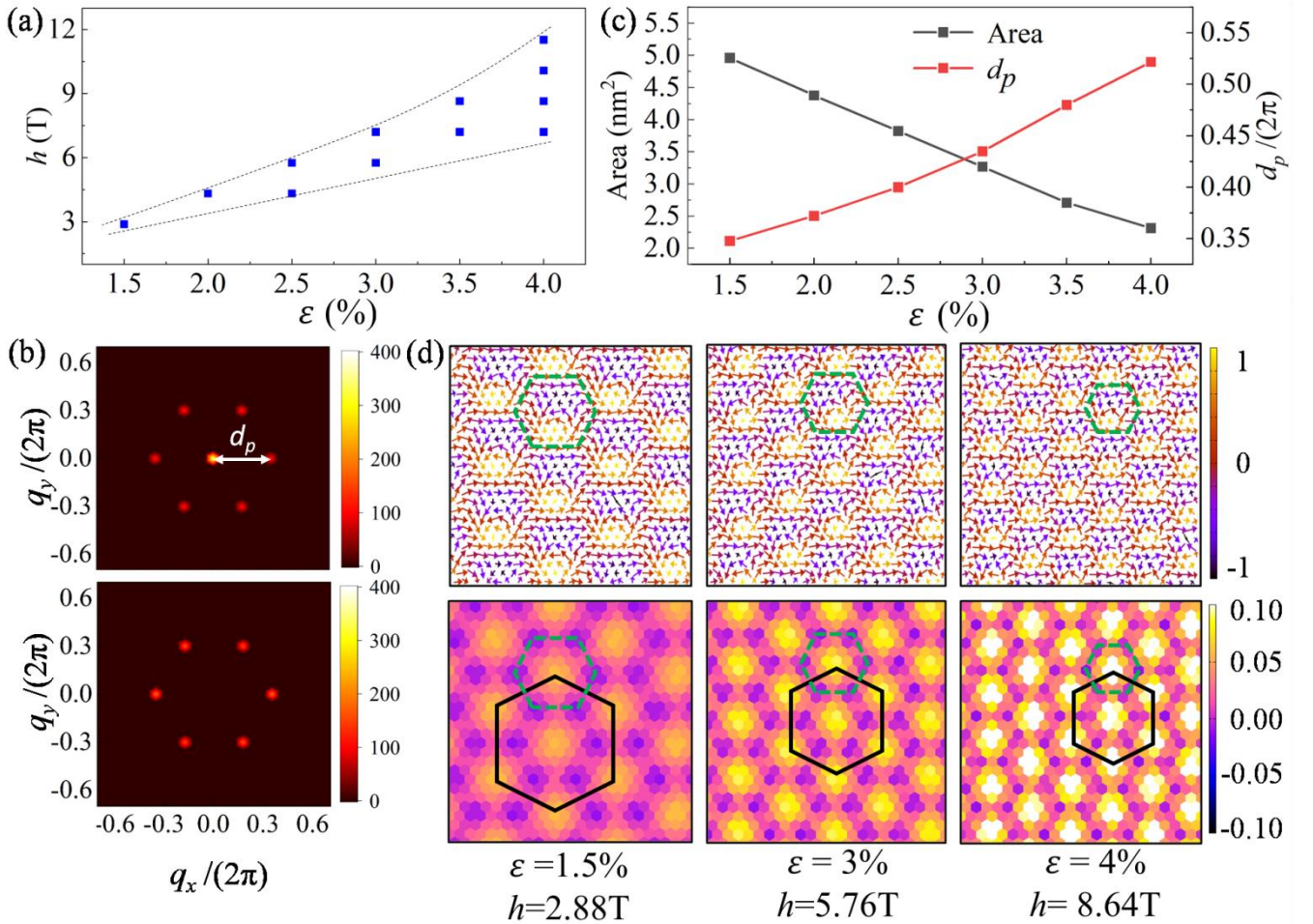


Fig. 4 The bimeron states in CoCl_2 monolayer with tensile strain from MC simulation. (a) The h - ε phase diagram. Here the blue squares

show the parameter points where the bimeron states exist stably. (b) The intensity plots of the spin structure factor at $\varepsilon = 1.5\%$: $S^x(\mathbf{q})$ in the top panel, $S^y(\mathbf{q})+S^z(\mathbf{q})$ in the bottom panel, where d_p denotes the distance between the peaks at corner and center. (c) The area of a single bimeron and d_p as a function of the tensile strain. (d) The real-space bimeron lattices under different tensile strains. The top panels display spin configurations where the vector represents the spin projection onto the xy plane and the color presents its z component. The bottom panels exhibit the local topology charge density and the color refers to the value of $\rho(r)$. The dashed small hexagon outlines the region of one bimeron, and the solid large hexagon presents the lattice formed by bimerons.

For CoBr₂ monolayer, the situation is much more complicated than CoCl₂. As plotted in Fig. 5(a), J_1 declines first and then ascends. When ε reaches -3.5% , J_1 falls to the minimum (-7.184meV), i.e. the strongest FM value. Meanwhile, the Co-Br-Co bond angle θ decreases with increasing ε . It reaches 89.92° at $\varepsilon = -3.5\%$, which is extremely close to 90° , just corresponding to the strongest J_1 , in agreement with the GKA rules [89-91]. Meanwhile, the electronic density between Co and Br ions increases when the strain is strengthened up to -3.5% [inset in Fig. 5(a)], which also implies the enhancement of p - d hybridization. On the other hand, it is noteworthy that J_2 and J_3 exhibit intriguing variations, that is, J_2 swaps place with J_3 . J_3 declines from 1.910 to 0.117 meV, while J_2 rises from 0.110 to 2.257 meV when ε is compressed to -4% . Compared to the normal response of J_2 and J_3 to strain in CoCl₂, their subtle variations in CoBr₂ may result from the $4p$ orbitals of Br, which are more spatially expanded than $3p$ orbitals of Cl. As shown in Fig. 5(b), although $|J_2/J_1|$ increases but $|J_3/J_1|$ decreases, the ratio $|(J_2+J_3)/J_1|$ declines as a function of ε , which means that the frustration is gradually weakened by compressive strain. In addition, the magnetic anisotropic coefficient k of CoBr₂ monolayer also decreases with increasing ε , but it always keeps in-plane [Fig. 5(c)].

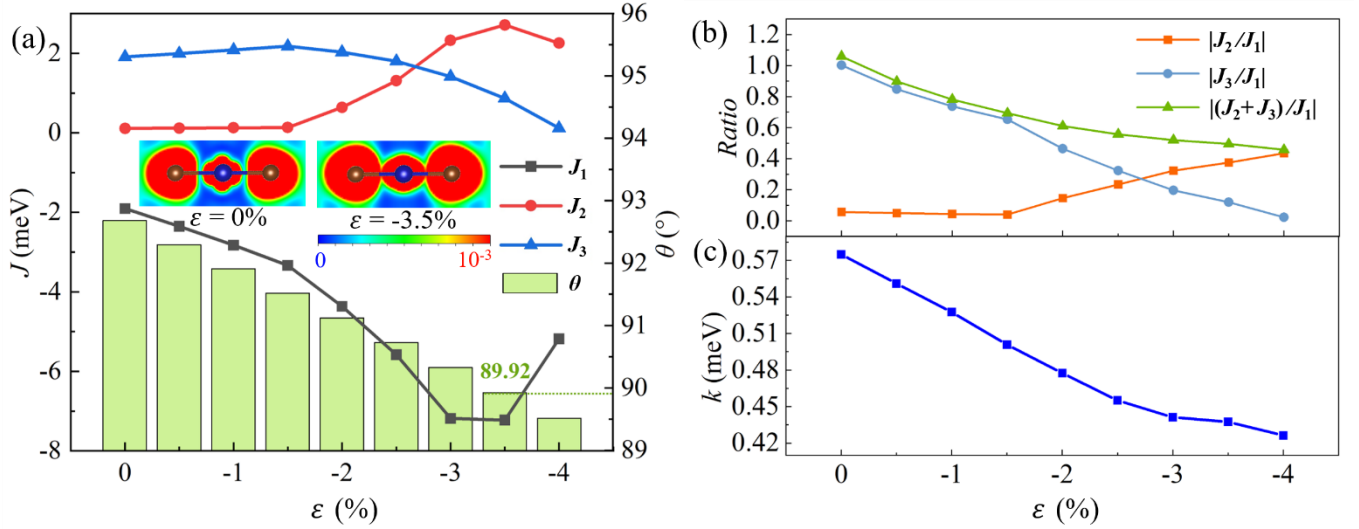


Fig. 5 The effect of compressive strain on CoBr₂ monolayer. (a) The exchange coefficients J_1 , J_2 , J_3 and Co-Br-Co bond angle θ , (b) The ratios $|J_2/J_1|$, $|J_3/J_1|$, $|(J_2+J_3)/J_1|$, and (c) magnetic anisotropic coefficient k as a function of the compressive strain. The insets in (a) present electronic density profiles at $\varepsilon = 0\%$ and -3.5% (cut in the plane of Br-Co-Br bond). The blue and brown balls represent Co and Br atoms, respectively.

The MC simulation of the monolayer CoBr₂ under an in-plane magnetic field demonstrates that high-density bimerons can exist in the form of triangular lattice without any strain, as shown in Fig. 6(a) and 6(d). At this time, the area of each bimeron can be as small as 2.281 nm^2 [Fig. 6(c)]. These frustration-induced bimerons can be stabilized at finite temperatures [94]. With the compressive strain increasing up to -4% , the bimeron lattice may exist stably under an appropriate magnetic field, but its h -window shrinks [Fig. 6(a)]. Meanwhile, the density of bimerons gradually decreases due to the suppression of frustration [Fig. 6(d)]. Correspondingly, the area of a single bimeron expands and the spin

structure factor presents d_p decreasing, as presented in Fig. 6(c). It is interesting that when J_2 is larger than J_3 , namely, the strain is stronger than -3%, the orientation of the hexagonal bimeron lattice begins to rotate slightly, as plotted in Fig. 6(d). When the strain reaches -4%, the whole bimeron lattice has successfully rotated 30°. Corresponding to the spin configuration, the peaks of spin structure factor also rotate 30° [Fig. 6(b)]. This rotation of whole bimeron lattice just results from the variation of J_2 and J_3 , namely J_2 swaps place with J_3 when compressive strain is enhanced from -3% to -4% as shown in Fig. 5(a). Different from the rotation of skyrmion lattice induced by electric currents and thermal gradients in MnSi [96] or by electric field in Cu₂OSeO₃ [97], this strain-controlled rotation of bimeron lattice has not been reported, to the best of our knowledge. Therefore, the compressive strain can be applied to control frustration in CoBr₂ monolayer to tune not only the density of bimerons but also the orientation of bimeron lattice.

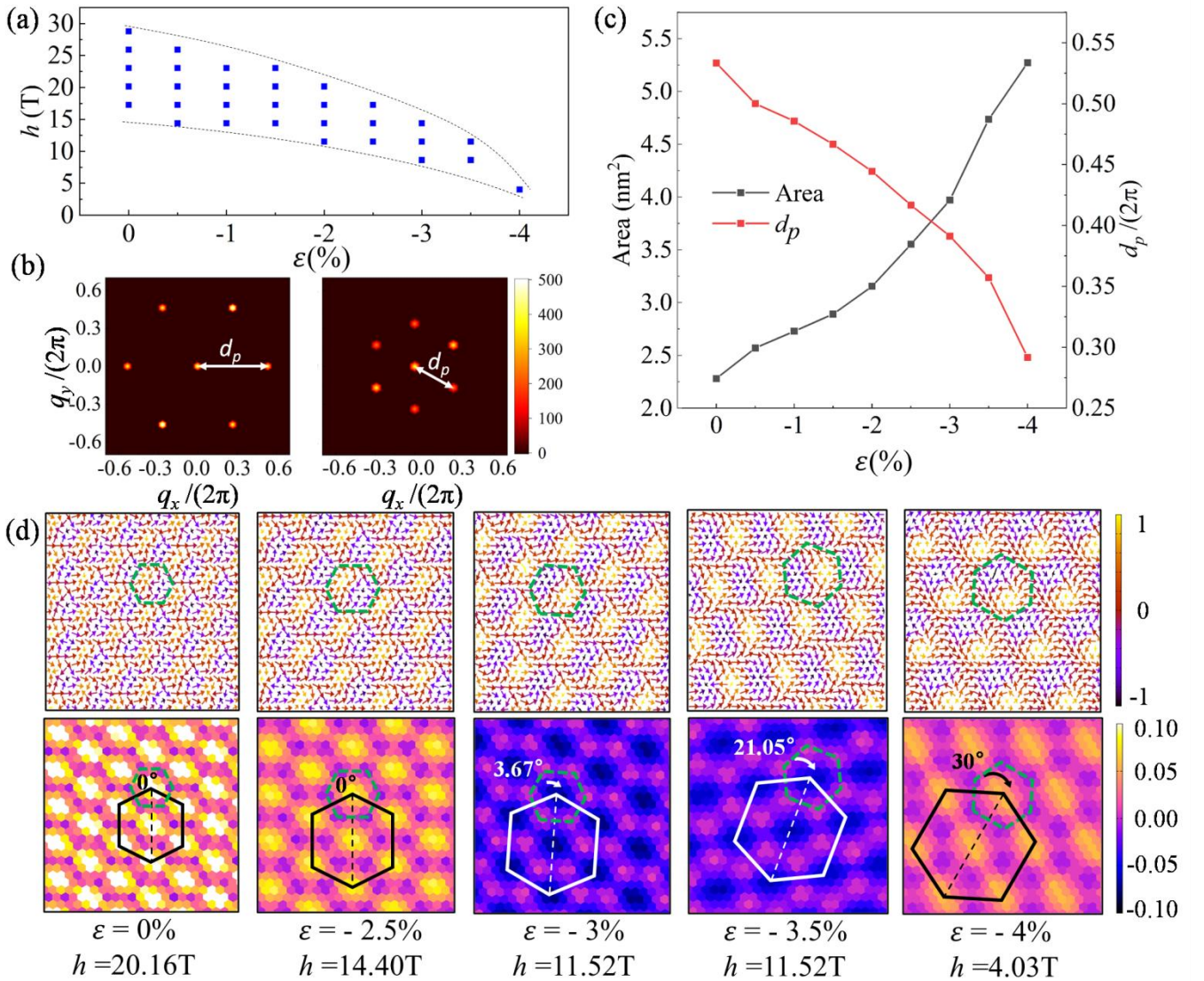


Fig. 6 The bimeron states in CoBr₂ monolayer with compressive strain from MC simulation (a) The h - ϵ phase diagram. Here the blue squares show the parameter points where the bimeron states exist stably. (b) The intensity plots of the spin structure factor $S^x(\mathbf{q})+S^y(\mathbf{q})+S^z(\mathbf{q})$ for $\epsilon = 0\%$ in the left panel and $\epsilon = -4\%$ in the right panel. (c) The area of a single bimeron and d_p as a function of the compressive strain. (d) The real-space bimeron lattices under different compressive strains. The top panels display spin configurations where the vector represents the spin projection onto the xy plane and the color presents its z component. The bottom panels exhibit the local topology charge density and the

color refers to the value of $\rho(\mathbf{r})$. The frustration-induced bimeron lattices with opposite topological charges are degenerate in energy, so they appear randomly. The dashed small hexagon outlines the region of one bimeron, and the solid large hexagon presents the lattice formed by bimerons.

4 Conclusion

In summary, by using first-principles calculations and Monte Carlo simulations, the noncollinear magnetic textures in CoX_2 ($X = \text{Cl}, \text{Br}$) monolayers are investigated. The calculation indicates that the frustration-induced bimeron lattice could exist under appropriate magnetic field in these 2D monolayers, and biaxial strain provides an effective method to tune these magnetic textures via controlling frustration. For CoCl_2 monolayer with dominant ferromagnetism, tensile strain could be applied to generate bimeron lattice. Furthermore, it reduces the size of each bimeron and increases the density of bimeron lattice. For CoBr_2 monolayer, bimeron lattice exists even without the application of strain, and it can be modulated by compressive strain. In particular, an exotic strain-controlled rotation of bimeron lattice is revealed in this vdW monolayer. The superiority in size and tunability of these frustration-induced bimerons will trigger special interest to the investigation of the topological magnetic textures in 2D materials, and help for searching more candidates for much-desired spintronic devices with high storage density and low power consumption.

Acknowledgements

We thank N. Ding, H. P. You and J. Chen for useful discussions. This work is supported by the Natural Science Foundation of Jiangsu Province (BK20221451), the National Natural Science Foundation of China (11834002, 12274070) and the Fundamental Research Funds for the Central Universities (2242022K40027). Most calculations were done on the Big Data Computing Center of Southeast University.

References

- [1] D.L. Duong, S.J. Yun, Y.H. Lee, van der Waals layered materials: opportunities and challenges, *ACS Nano*, 11 (2017) 11803-11830.
- [2] R. Bian, C. Li, Q. Liu, G. Cao, Q. Fu, P. Meng, J. Zhou, F. Liu, Z. Liu, Recent progress in the synthesis of novel two-dimensional van der Waals materials, *Natl. Sci. Rev.*, 9 (2022) nwab164.
- [3] K.S. Burch, D. Mandrus, J.G. Park, Magnetism in two-dimensional van der Waals materials, *Nature*, 563 (2018) 47-52.
- [4] S. Zhang, R. Xu, N. Luo, X. Zou, Two-dimensional magnetic materials: structures, properties and external controls, *Nanoscale*, 13 (2021) 1398-1424.
- [5] S. Zhang, H. Wu, L. Yang, G. Zhang, Y. Xie, L. Zhang, W. Zhang, H. Chang, Two-dimensional magnetic atomic crystals, *Mater. Horiz.*, 9 (2022) 559-576.
- [6] C. Gong, L. Li, Z. Li, H. Ji, A. Stern, Y. Xia, T. Cao, W. Bao, C. Wang, Y. Wang, Z.Q. Qiu, R.J. Cava, S.G. Louie, J. Xia, X. Zhang, Discovery of intrinsic ferromagnetism in two-dimensional van der Waals crystals, *Nature*, 546 (2017) 265-269.
- [7] B. Huang, G. Clark, E. Navarro-Moratalla, D.R. Klein, R. Cheng, K.L. Seyler, D. Zhong, E. Schmidgall, M.A. McGuire, D.H. Cobden, W. Yao, D. Xiao, P. Jarillo-Herrero, X. Xu, Layer-dependent ferromagnetism in a van der Waals crystal down to the monolayer limit, *Nature*, 546 (2017) 270-273.
- [8] Y. Deng, Y. Yu, Y. Song, J. Zhang, N.Z. Wang, Z. Sun, Y. Yi, Y.Z. Wu, S. Wu, J. Zhu, J. Wang, X.H. Chen, Y. Zhang, Gate-tunable room-temperature ferromagnetism in two-dimensional Fe_3GeTe_2 , *Nature*, 563 (2018) 94-99.
- [9] D.J. O'Hara, T. Zhu, A.H. Trout, A.S. Ahmed, Y.K. Luo, C.H. Lee, M.R. Brenner, S. Rajan, J.A. Gupta, D.W. McComb, R.K. Kawakami, Room Temperature Intrinsic Ferromagnetism in Epitaxial Manganese Selenide Films in the Monolayer Limit, *Nano Lett.*, 18 (2018) 3125-3131.

- [10] J.U. Lee, S. Lee, J.H. Ryoo, S. Kang, T.Y. Kim, P. Kim, C.H. Park, J.G. Park, H. Cheong, Ising-Type Magnetic Ordering in Atomically Thin FePS₃, *Nano Lett.*, 16 (2016) 7433-7438.
- [11] J.J. Xian, C. Wang, J.H. Nie, R. Li, M. Han, J. Lin, W.H. Zhang, Z.Y. Liu, Z.M. Zhang, M.P. Miao, Y. Yi, S. Wu, X. Chen, J. Han, Z. Xia, W. Ji, Y.S. Fu, Spin mapping of intralayer antiferromagnetism and field-induced spin reorientation in monolayer CrTe₂, *Nat. Commun.*, 13 (2022) 257.
- [12] B. Wang, X. Zhang, Y. Zhang, S. Yuan, Y. Guo, S. Dong, J. Wang, Prediction of a two-dimensional high-T_c f-electron ferromagnetic semiconductor, *Mater. Horiz.*, 7 (2020) 1623-1630.
- [13] N. Miao, B. Xu, L. Zhu, J. Zhou, Z. Sun, 2D Intrinsic Ferromagnets from van der Waals Antiferromagnets, *J. Am. Chem. Soc.*, 140 (2018) 2417-2420.
- [14] Z. Chen, X. Fan, Z. Shen, Z. Luo, D. Yang, S. Ma, Two-dimensional intrinsic ferromagnetic half-metals: monolayers Mn₃X₄ (X = Te, Se, S), *J. Mater. Sci.*, 55 (2020) 7680-7690.
- [15] Z. Guan, H. Hu, X. Shen, P. Xiang, N. Zhong, J. Chu, C. Duan, Recent Progress in Two-Dimensional Ferroelectric Materials, *Adv. Electron. Mater.*, 6 (2020) 1900818.
- [16] J. Chu, Y. Wang, X. Wang, K. Hu, G. Rao, C. Gong, C. Wu, H. Hong, X. Wang, K. Liu, C. Gao, J. Xiong, 2D Polarized Materials: Ferromagnetic, Ferrovalley, Ferroelectric Materials, and Related Heterostructures, *Adv. Mater.*, 33 (2021) 2004469.
- [17] E. Elahi, G. Dastgeer, G. Nazir, S. Nisar, M. Bashir, H. Akhter Qureshi, D.-k. Kim, J. Aziz, M. Aslam, K. Hussain, M.A. Assiri, M. Imran, A review on two-dimensional (2D) magnetic materials and their potential applications in spintronics and spin-caloritronic, *Comput. Mater. Sci.*, 213 (2022) 111670.
- [18] Y. Gao, Y.-Y. Zhang, J.-T. Sun, L. Zhang, S. Zhang, S. Du, Quantum anomalous Hall effect in two-dimensional Cu-dicyanobenzene coloring-triangle lattice, *Nano Res.*, 13 (2020) 1571-1575.
- [19] B. Göbel, I. Mertig, O.A. Tretiakov, Beyond skyrmions: Review and perspectives of alternative magnetic quasiparticles, *Phys. Rep.*, 895 (2021) 1-28.
- [20] K. Everschor-Sitte, J. Masell, R.M. Reeve, M. Kläui, Perspective: Magnetic skyrmions—Overview of recent progress in an active research field, *J. Appl. Phys.*, 124 (2018) 240901.
- [21] X. Yao, S. Dong, Stabilization and modulation of the topological magnetic phase with a Z₂-vortex lattice in the Kitaev-Heisenberg honeycomb model: The key role of the third-nearest-neighbor interaction, *Phys. Rev. B*, 98 (2018) 054413.
- [22] S. Li, W. Kang, X. Zhang, T. Nie, Y. Zhou, K.L. Wang, W. Zhao, Magnetic skyrmions for unconventional computing, *Mater. Horiz.*, 8 (2021) 854-868.
- [23] X. Zhang, Y. Zhou, K. Mee Song, T.E. Park, J. Xia, M. Ezawa, X. Liu, W. Zhao, G. Zhao, S. Woo, Skyrmion-electronics: writing, deleting, reading and processing magnetic skyrmions toward spintronic applications, *J. Phys. Condens. Matter*, 32 (2020) 143001.
- [24] A. Fert, N. Reyren, V. Cros, Magnetic skyrmions: advances in physics and potential applications, *Nat. Rev. Mater.*, 2 (2017) 17031.
- [25] W. Sun, W. Wang, H. Li, G. Zhang, D. Chen, J. Wang, Z. Cheng, Controlling bimerons as skyrmion analogues by ferroelectric polarization in 2D van der Waals multiferroic heterostructures, *Nat. Commun.*, 11 (2020) 5930.
- [26] M. Ezawa, Compact merons and skyrmions in thin chiral magnetic films, *Phys. Rev. B*, 83 (2011) 100408.
- [27] R. Silva, L. Secchin, W. Moura-Melo, A. Pereira, R. Stamps, Emergence of skyrmion lattices and bimerons in chiral magnetic thin films with nonmagnetic impurities, *Phys. Rev. B*, 89 (2014) 054434.
- [28] A.O. Leonov, C. Pappas, I.I. Smalyukh, Field-driven metamorphoses of isolated skyrmions within the conical state of cubic helimagnets, *Phys. Rev. B*, 104 (2021) 064432.
- [29] H.D. Rosales, F.A.G. Albarracín, P. Pujol, L.D. Jaubert, Skyrmion Fluid and Bimeron Glass Protected by a Chiral Spin Liquid on a Kagome Lattice, *Phys. Rev. Lett.*, 130 (2023) 106703.
- [30] B. Göbel, A. Mook, J. Henk, I. Mertig, O.A. Tretiakov, Magnetic bimerons as skyrmion analogues in in-plane magnets, *Phys. Rev. B*, 99 (2019) 060407.

- [31] R. Zarzuela, V.K. Bharadwaj, K.-W. Kim, J. Sinova, K. Everschor-Sitte, Stability and dynamics of in-plane skyrmions in collinear ferromagnets, *Phys. Rev. B*, 101 (2020) 054405.
- [32] A. Leonov, I. Kézsmárki, Asymmetric isolated skyrmions in polar magnets with easy-plane anisotropy, *Phys. Rev. B*, 96 (2017) 014423.
- [33] R. Murooka, A.O. Leonov, K. Inoue, J.-i. Ohe, Current-induced shuttlecock-like movement of non-axisymmetric chiral skyrmions, *Sci. Rep.*, 10 (2020) 396.
- [34] Y.A. Kharkov, O.P. Sushkov, M. Mostovoy, Bound States of Skyrmions and Merons near the Lifshitz Point, *Phys. Rev. Lett.*, 119 (2017) 207201.
- [35] G. Chen, S.P. Kang, C. Ophus, A.T. N'Diaye, H.Y. Kwon, R.T. Qiu, C. Won, K. Liu, Y. Wu, A.K. Schmid, Out-of-plane chiral domain wall spin-structures in ultrathin in-plane magnets, *Nat. Commun.*, 8 (2017) 15302.
- [36] N. Gao, S. Je, M. Im, J.W. Choi, M. Yang, Q. Li, T.Y. Wang, S. Lee, H. Han, K. Lee, W. Chao, C. Hwang, J. Li, Z.Q. Qiu, Creation and annihilation of topological meron pairs in in-plane magnetized films, *Nat. Commun.*, 10 (2019) 5603.
- [37] H. Jani, J.C. Lin, J. Chen, J. Harrison, F. Maccherozzi, J. Schäd, S. Prakash, C.B. Eom, A. Ariando, T. Venkatesan, P.G. Radaelli, Antiferromagnetic half-skyrmions and bimerons at room temperature, *Nature*, 590 (2021) 74-79.
- [38] X.Z. Yu, N. Kanazawa, Y. Onose, K. Kimoto, W.Z. Zhang, S. Ishiwata, Y. Matsui, Y. Tokura, Near room-temperature formation of a skyrmion crystal in thin-films of the helimagnet FeGe, *Nat. Mater.*, 10 (2011) 106-109.
- [39] X. Yao, Y. Wang, S. Dong, Noncollinear topological textures in two-dimensional van der Waals materials: From magnetic to polar systems, *Int. J. Mod. Phys. B*, 35 (2021) 2130004.
- [40] M.G. Han, J.A. Garlow, Y. Liu, H. Zhang, J. Li, D. DiMarzio, M.W. Knight, C. Petrovic, D. Jariwala, Y. Zhu, Topological Magnetic-Spin Textures in Two-Dimensional van der Waals Cr₂Ge₂Te₆, *Nano Lett.*, 19 (2019) 7859-7865.
- [41] B. Ding, Z. Li, G. Xu, H. Li, Z. Hou, E. Liu, X. Xi, F. Xu, Y. Yao, W. Wang, Observation of Magnetic Skyrmion Bubbles in a van der Waals Ferromagnet Fe₃GeTe₂, *Nano Lett.*, 20 (2020) 868-873.
- [42] H. Zhang, D. Raftrey, Y.-T. Chan, Y.-T. Shao, R. Chen, X. Chen, X. Huang, J.T. Reichenadter, K. Dong, S. Susarla, Room-temperature skyrmion lattice in a layered magnet (Fe_{0.5}Co_{0.5})₅GeTe₂, *Sci. Adv.*, 8 (2022) eabm7103.
- [43] X. Yao, D. Hu, S. Dong, Modulation of skyrmionic magnetic textures in two dimensional vdW materials and their heterostructures, *Iscience*, (2023).
- [44] C. Xu, J. Feng, S. Prokhorenko, Y. Nahas, H. Xiang, L. Bellaïche, Topological spin texture in Janus monolayers of the chromium trihalides Cr(I, X)₃, *Phys. Rev. B*, 101 (2020) 060404.
- [45] C. Xu, P. Chen, H. Tan, Y. Yang, H. Xiang, L. Bellaïche, Electric-Field Switching of Magnetic Topological Charge in Type-I Multiferroics, *Phys. Rev. Lett.*, 125 (2020) 037203.
- [46] Q. Cui, Y. Zhu, J. Jiang, J. Liang, D. Yu, P. Cui, H. Yang, Ferroelectrically controlled topological magnetic phase in a Janus-magnet-based multiferroic heterostructure, *Physical Review Research*, 3 (2021) 043011.
- [47] Z. He, K. Dou, W. Du, Y. Dai, B. Huang, Y. Ma, Multiple Topological Magnetism in van der Waals Heterostructure of MnTe₂/ZrS₂, *Nano Lett.*, 23 (2023) 312-318.
- [48] W. Sun, W. Wang, H. Li, X. Li, Z. Yu, Y. Bai, G. Zhang, Z. Cheng, LaBr₂ bilayer multiferroic moiré superlattice with robust magnetoelectric coupling and magnetic bimerons, *NPJ Comput. Mater.*, 8 (2022) 159.
- [49] T. Okubo, S. Chung, H. Kawamura, Multiple-q states and the skyrmion lattice of the triangular-lattice Heisenberg antiferromagnet under magnetic fields, *Phys. Rev. Lett.*, 108 (2012) 017206.
- [50] A.O. Leonov, M. Mostovoy, Multiply periodic states and isolated skyrmions in an anisotropic frustrated magnet, *Nat. Commun.*, 6 (2015) 8275.
- [51] X. Yao, S. Dong, Vector vorticity of skyrmionic texture: An internal degree of freedom tunable by magnetic field, *Phys. Rev. B*, 105 (2022) 014444.
- [52] X. Yao, J. Chen, S. Dong, Controlling the helicity of magnetic skyrmions by electrical field in frustrated magnets, *New J. Phys.*, 22 (2020) 083032.
- [53] Y. Tokura, N. Kanazawa, Magnetic Skyrmion Materials, *Chem. Rev.*, 121 (2021) 2857-2897.

- [54] T. Kurumaji, T. Nakajima, M. Hirschberger, A. Kikkawa, Y. Yamasaki, H. Sagayama, H. Nakao, Y. Taguchi, T.-h. Arima, Y. Tokura, Skyrmion lattice with a giant topological Hall effect in a frustrated triangular-lattice magnet, *Science*, 365 (2019) 914-918.
- [55] D. Amoroso, P. Barone, S. Picozzi, Spontaneous skyrmionic lattice from anisotropic symmetric exchange in a Ni-halide monolayer, *Nat. Commun.*, 11 (2020) 5784.
- [56] X. Zhang, J. Xia, L. Shen, M. Ezawa, O.A. Tretiakov, G. Zhao, X. Liu, Y. Zhou, Static and dynamic properties of bimerons in a frustrated ferromagnetic monolayer, *Phys. Rev. B*, 101 (2020) 144435.
- [57] G. Kresse, J. Furthmüller, Efficient iterative schemes for ab initio total-energy calculations using a plane-wave basis set, *Phys. Rev. B*, 54 (1996) 11169.
- [58] P.E. Blochl, Projector augmented-wave method, *Phys. Rev. B*, 50 (1994) 17953.
- [59] J. P. Perdew, K. Burke, M. Ernzerhof, Generalized gradient approximation made simple, *Phys. Rev. Lett.*, 77 (1996) 3865.
- [60] A. Tkatchenko, R.A. DiStasio, Jr., R. Car, M. Scheffler, Accurate and efficient method for many-body van der Waals interactions, *Phys. Rev. Lett.*, 108 (2012) 236402.
- [61] A. Ambrosetti, A.M. Reilly, R.A. DiStasio, Jr., A. Tkatchenko, Long-range correlation energy calculated from coupled atomic response functions, *J. Chem. Phys.*, 140 (2014) 18A508.
- [62] X. Gonze, C. Lee, Dynamical matrices, Born effective charges, dielectric permittivity tensors, and interatomic force constants from density-functional perturbation theory, *Phys. Rev. B*, 55 (1997) 10355.
- [63] A. Togo, I. Tanaka, First principles phonon calculations in materials science, *Scr. Mater.*, 108 (2015) 1-5.
- [64] M. Creutz, Overrelaxation and Monte Carlo simulation, *Phys. Rev. D*, 36 (1987) 515-519.
- [65] L. Lee, A. Young, Large-scale Monte Carlo simulations of the isotropic three-dimensional Heisenberg spin glass, *Phys. Rev. B*, 76 (2007) 024405.
- [66] B. Berg, M. Lüscher, Definition and statistical distributions of a topological number in the lattice O (3) σ -model, *Nucl. Phys. B*, 190 (1981) 412-424.
- [67] M.A. Michael, Crystal and Magnetic Structures in Layered, Transition Metal Dihalides and Trihalides, *Crystals*, 7 (2017) 121.
- [68] H. Grime, J.A. Santos, The Structure and Colour of Anhydrous Cobalt Chloride, CoCl_2 , at Room and very Low Temperatures, *Z. Kristallogr. Cryst. Mater.*, 88 (1934) 136-141.
- [69] A. Ferrari, F. Giorgi, La struttura cristallina dei bromuri di metalli bivalenti, *Atti Accad. Naz. Lincei Cl. Sci. Fis. Mat. Nat. Rend.*, 9 (1929) 1134-1140.
- [70] J.A. Barreda-Argueso, L. Nataf, F. Aguado, I. Hernandez, J. Gonzalez, A. Otero-de-la-Roza, V. Luana, Y. Jia, C. Jin, B. Kim, K. Kim, B.I. Min, W. Heribert, A.P. Jephcoat, F. Rodriguez, Pressure-induced spin transition and site-selective metallization in CoCl_2 , *Sci. Rep.*, 9 (2019) 5448.
- [71] M.K. Wilkinson, J.W. Cable, E.O. Wollan, W.C. Koehler, Neutron Diffraction Investigations of the Magnetic Ordering in FeBr_2 , CoBr_2 , FeCl_2 , and CoCl_2 , *Phys. Rev.*, 113 (1959) 497-507.
- [72] P. Chen, J.Y. Zou, B.G. Liu, Intrinsic ferromagnetism and quantum anomalous Hall effect in a CoBr_2 monolayer, *Phys. Chem. Chem. Phys.*, 19 (2017) 13432-13437.
- [73] H.Y. Lv, W.J. Lu, X. Luo, X.B. Zhu, Y.P. Sun, Strain- and carrier-tunable magnetic properties of a two-dimensional intrinsically ferromagnetic semiconductor: CoBr_2 monolayer, *Phys. Rev. B*, 99 (2019) 134416.
- [74] N. Mounet, M. Gibertini, P. Schwaller, D. Campi, A. Merkys, A. Marrazzo, T. Sohler, I.E. Castelli, A. Cepellotti, G. Pizzi, N. Marzari, Two-dimensional materials from high-throughput computational exfoliation of experimentally known compounds, *Nat. Nanotechnol.*, 13 (2018) 246-252.
- [75] E. Torun, H. Sahin, S.K. Singh, F.M. Peeters, Stable half-metallic monolayers of FeCl_2 , *Appl. Phys. Lett.*, 106 (2015) 192404.
- [76] Y. Feng, X. Wu, J. Han, G. Gao, Robust half-metallicities and perfect spin transport properties in 2D transition metal dichlorides, *J. Mater. Chem. C*, 6 (2018) 4087-4094.
- [77] J. Luo, G. Xiang, Y. Tang, K. Ou, X. Chen, The electric and magnetic properties of novel two-dimensional MnBr_2 and MnI_2 from first-principles calculations, *J. Appl. Phys.*, 128 (2020) 113901.

- [78] H.-X. Cheng, J. Zhou, W. Ji, Y.-N. Zhang, Y.-P. Feng, Two-dimensional intrinsic ferrovalley GdI₂ with large valley polarization, *Phys. Rev. B*, 103 (2021) 125121.
- [79] W. Wang, S. Dai, X. Li, J. Yang, D.J. Srolovitz, Q. Zheng, Measurement of the cleavage energy of graphite, *Nat. Commun.*, 6 (2015) 7853.
- [80] V. Wang, N. Xu, J.-C. Liu, G. Tang, W.-T. Geng, VASPKIT: A user-friendly interface facilitating high-throughput computing and analysis using VASP code, *Comput. Phys. Commun.*, 267 (2021) 108033.
- [81] R. Li, Q. Shao, E. Gao, Z. Liu, Elastic anisotropy measure for two-dimensional crystals, *Extreme Mech. Lett.*, 34 (2020) 100615.
- [82] R.C. Andrew, R.E. Mapasha, A.M. Ukpong, N. Chetty, Mechanical properties of graphene and boronitrene, *Phys. Rev. B*, 85 (2012) 125428.
- [83] C. Lee, X. Wei, J.W. Kysar, J. Hone, Measurement of the elastic properties and intrinsic strength of monolayer graphene, *Science*, 321 (2008) 385-388.
- [84] T.J. Booth, P. Blake, R.R. Nair, D. Jiang, E.W. Hill, U. Bangert, A. Bleloch, M. Gass, K.S. Novoselov, M.I. Katsnelson, Macroscopic graphene membranes and their extraordinary stiffness, *Nano Lett.*, 8 (2008) 2442-2446.
- [85] A.S. Botana, M.R. Norman, Electronic structure and magnetism of transition metal dihalides: Bulk to monolayer, *Phys. Rev. Mater.*, 3 (2019) 044001.
- [86] M. Mohylna, F.G. Albarracín, M. Žukovič, H. Rosales, Spontaneous antiferromagnetic skyrmion/antiskyrmion lattice and spiral spin-liquid states in the frustrated triangular lattice, *Phys. Rev. B*, 106 (2022) 224406.
- [87] A. Aldarawsheh, M. Sallermann, M. Abusaa, S. Lounis, A spin model for intrinsic antiferromagnetic skyrmions on a triangular lattice, *Front. Phys.*, 11 (2023) 1175317.
- [88] T. Shimokawa, T. Okubo, H. Kawamura, Multiple-q states of the J₁-J₂ classical honeycomb-lattice Heisenberg antiferromagnet under a magnetic field, *Phys. Rev. B*, 100 (2019) 224404.
- [89] J.B. Goodenough, Theory of the Role of Covalence in the Perovskite-Type Manganites [La, M(II)]MnO₃, *Phys. Rev.*, 100 (1955) 564-573.
- [90] J. Kanamori, Superexchange interaction and symmetry properties of electron orbitals, *J. Phys. Chem. Solids*, 10 (1959) 87-98.
- [91] P.W. Anderson, New Approach to the Theory of Superexchange Interactions, *Phys. Rev.*, 115 (1959) 2-13.
- [92] N. Sivadas, M.W. Daniels, R.H. Swendsen, S. Okamoto, D. Xiao, Magnetic ground state of semiconducting transition-metal trichalcogenide monolayers, *Phys. Rev. B*, 91 (2015) 235425.
- [93] J.L. Lado, J. Fernández-Rossier, On the origin of magnetic anisotropy in two dimensional CrI₃, *2D Mater.*, 4 (2017) 035002.
- [94] S. Hayami, In-plane magnetic field-induced skyrmion crystal in frustrated magnets with easy-plane anisotropy, *Phys. Rev. B*, 103 (2021) 224418.
- [95] X.Z. Yu, W. Koshibae, Y. Tokunaga, K. Shibata, Y. Taguchi, N. Nagaosa, Y. Tokura, Transformation between meron and skyrmion topological spin textures in a chiral magnet, *Nature*, 564 (2018) 95-98.
- [96] F. Jonietz, S. Mühlbauer, C. Pfleiderer, A. Neubauer, W. Münzer, A. Bauer, T. Adams, R. Georgii, P. Böni, R.A. Duine, Spin transfer torques in MnSi at ultralow current densities, *Science*, 330 (2010) 1648-1651.
- [97] J.S. White, K. Prsa, P. Huang, A.A. Omrani, I. Zivkovic, M. Bartkowiak, H. Berger, A. Magrez, J.L. Gavilano, G. Nagy, J. Zang, H.M. Ronnow, Electric-field-induced Skyrmion distortion and giant lattice rotation in the magnetoelectric insulator Cu₂OSeO₃, *Phys. Rev. Lett.*, 113 (2014) 107203.